THE JOURNAL OF PHYSICAL CHEMISTRY C

pubs.acs.org/JPCC Article

Impact of Bis(imino)pyridine Ligands on Mesoscale Properties of CdSe/ZnS Quantum Dots

Mark D. Bartolo, Ryan P. Brisbin, James C. Fettinger, Sayantani Ghosh, and Ryan D. Baxter*

Cite This: J. Phys. Chem. C 2020, 124, 22677−22683 Read Online

ABSTRACT: We investigate the effect of surface modification of CdSe/ZnS quantum dots (QDs) with bis(imino)pyridine (BIP) ligands. BIPs are a class of redox noninnocent ligands known to facilitate charge transfer in base metals on the molecular scale, but their behavior in nano- to mesoscale systems has been largely unexplored. Using electron microscopy, crystallography, and ultrafast spectroscopy, we reveal that structure-specific $\pi-\pi$ stacking of the BIP molecules alters interdot separation in QD films, thereby leading to changes in optical and electronic properties. The three variations used are unsubstituted (BIP-H), dimethyl (BIP-Me), and diisopropyl (BIP-Ipr) BIP, and when compared with the native octadecylamine ligand, we find that both energy and charge transfer efficiencies between QDs are increased postligand exchange, the highest achieved through BIP-Ipr despite its larger unit cell volume. We further investigate charge transfer from QD films to conducting (indium tin oxide, ITO) and semiconducting (zinc oxide, ZnO) substrates using time-resolved spectroscopy and determine that the influence of the ligands is QD band gap-dependent. In QDs with a large band gap (2.3 eV), the BIP ligands facilitate charge transfer to both ITO and ZnO substrates, but in dots with a small band gap (1.9 eV), they pose a hindrance when ZnO is used, resulting in reduced recombination rates. These results highlight the importance of investigating multiple avenues in order to optimize surface modification of QDs based on the end goal. Finally, we verify that BIP ligands hasten the rate of QD photobrightening under continuous illumination, allowing the ensemble to achieve stable emission faster than in their native configuration. Our study sets the stage for novel charge transfer systems in the meso- and nanoscale, yielding a diverse selection of new surface ligands for applications such as conductive materials and energy production/storage devices employing QDs.

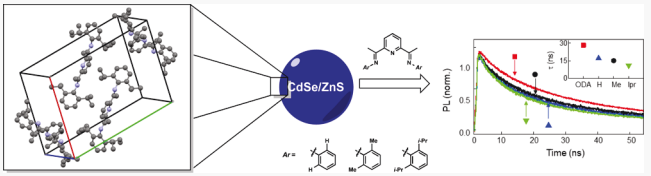

INTRODUCTION

Semiconducting quantum dots (QDs) are widely implemented in a variety of applications that leverage their size-tunable optical and electronic properties.[1−3] These include optoelectronic devices, such as, photodetectors,[4−6] light-emitting diodes,[7] and photovoltaics[8] among others, as well as devices for biomedical sensing[9,10] and diagnostics.[11,12] In order to optimize performance in these platforms, the treatment of QD surfaces is of critical importance, given the dots' large surface-to-volume ratios, and the one effective approach to surface passivation is via the use of organic ligands.[13−15] The most common among these are long-chain aliphatic hydrocarbons, which have been proven very successful in passivating surface defect-related trap states, thereby suppressing nonradiative recombination and stabilizing the QD core from photoinduced degradation, such as photodarkening and photo-oxidation.[16−19] However, as they insulate molecules they hinder transport of charge carriers within QD films, reducing the conductivity, and consequently, the performance in optoelectronic applications. Aromatic hydrocarbon molecules have facilitated interdot charge transport in QD films when used for surface functionalization owing to the presence of delocalized electrons, but these have occasionally altered the bandgap by reducing the excitonic confinement, especially when used in conjunction with metal complexes.[20−23] However, heterogenous charge transfer is a subject that garners interest not only in QD-based systems but across the scientific spectrum, from photovoltaics to electrode systems in batteries.[24] A specific type of charge transfer using organic ligands being heavily explored is for the purpose of advancing base metal catalysis and lowering the dependency on noble metals (palladium, rhodium, etc.,). That area is dominated by a class of organic molecules referred to as "redox non-innocent ligands" (RNI). These ligands have the capability to perform reversible charge transfers between a chelated metal and itself. This ability to participate in charge transfer allows metals like iron and cobalt to perform like rhodium and palladium, respectively, in catalytic reactions, through the process of acting as electron reservoirs.[25,26] This principle of RNI molecules acting as electron reservoirs is highly intriguing

Received: July 10, 2020
Revised: September 18, 2020
Published: September 21, 2020

https://dx.doi.org/10.1021/acs.jpcc.0c06335
J. Phys. Chem. C 2020, 124, 22677−22683

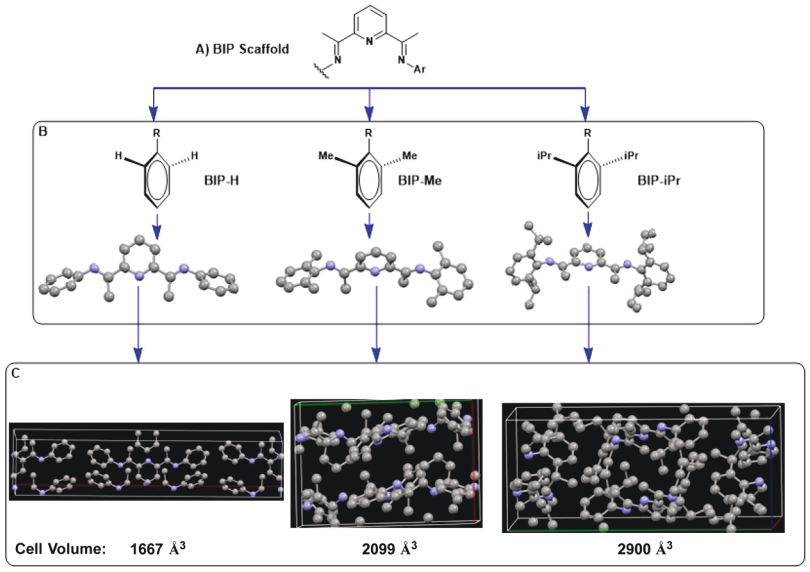

Figure 1. (A) Basic BIP scaffold, (B) three modular units used to design the ligands: BIP-H (unsubstituted BIP), BIP-Me (dimethyl BIP), and BIP-Ipr (diisopropyl BIP), and (C) unit cell structures formed by the ligands on crystallization.

and has yet to be applied on systems outside of the molecular scale. In this article, we demonstrate that RNI ligands can be utilized to modulate the optoelectronic properties of non-molecular scale systems such as semiconducting QDs through enhanced interdot charge and energy transfer.

We focus on a highly recognizable and well-behaved class of RNI ligands, the bis(imino)pyridine (BIP) scaffold (Figure 1A). The BIP scaffold is used for traditional organometallic chemistry[27−29] where it functions as the single-electron reservoir to facilitate two-electron processes with base metal catalysts. We use three variations of BIPs, unsubstituted (BIP-H), dimethyl (BIP-Me), and diisopropyl (BIP-Ipr) BIP (Figure 1B) to displace the native ligand, octadecylamine (ODA), of CdSe/ZnS core/shell QDs. Single crystals of each BIP are obtained to provide insights into how these ligands may orient/pack on the surface of the QDs. Then, using electron microscopy and ultrafast spectroscopy, we reveal that structure-specific $\pi-\pi$ stacking of the BIP ligands alters interdot separation in QD films, which correlates with the crystal lattice features of BIPs in the solid state (Figure 1C, unit cells of single-crystal data shown). This change in interdot separation leads to remarkable changes in both optical and electronic properties of the BIP-QD film in comparison to the native ligand. These include increases of both energy and charge transfer efficiencies between QDs post ligand exchange, the highest achieved with BIP-Ipr. We further investigate charge transfer from QD films to conducting (indium tin oxide, ITO) and semiconducting (zinc oxide, ZnO) substrates using time-resolved spectroscopy and determine that the influence of the BIP ligands is QD bandgap dependent. In QDs with a large band gap (2.3 eV), the BIP ligands facilitate charge transfer to both ITO and ZnO substrates, but in dots with a small band gap (1.9 eV), they pose a hindrance when ZnO is used, resulting in reduced recombination rates. Surface states also play a significant role in the photostability of colloidal QDs.[30,31] Photoinduced changes include photo brightening, photodarkening, and photo-oxidation, all of which result in changes in spectral emission intensity and wavelength over time. These shorten the shelf-life of QD samples and affect performance. The presence of ligands passivates the surface states and arrests these processes to varying degrees,[18,32,33] and therefore, it is important to investigate this aspect following a ligand exchange. We verify that BIP ligands hasten the rate of QD photobrightening under continuous illumination, allowing the ensemble to achieve stable emission faster than in their native configuration.

RESULTS AND DISCUSSION

To investigate intermolecular packing and size properties of QDs bound with organic BIP ligands, single crystal X-ray analyses were performed on each unbound ligand shown in Figure 1. Substitution at the 2- and 6-positions of the aniline subunits produced solid-state molecular geometries that minimize steric interaction between the aniline and central pyridine units, causing an out of plane tilt of aromatic rings that increases with substituent size (molecular geometries shown in **1B**, *i*-Pr > CH_3 > H for the degree of out of plane aromatic tilt). These results are consistent with previous reports of BIP ligands when chelated to a central metal in a Lewis basic fashion.[34] Although the geometric configuration of an single BIP ligand may be unsurprising, analysis of unit-cell packing is likely more informative for considering the bulk properties of numerous ligands creating a surface layer on the exterior of QDs. Because of the size disparity between QDs and BIP ligands, direct binding of the central pyridine to the QD surface is unlikely. Alternatively, induced dipole interactions between BIP π-systems and the QD surface could provide electrostatic attraction to promote an alternative mode of binding. Subsequent layers of BIP ligands extending from the QD surface would depend on intermolecular forces between BIP ligands to determine the overall size of the BIP-ligated QDs.

As shown in Figure 1C, the unsubstituted BIP-H ligand interacts primarily through the pre-existing dipole of the central pyridine unit, resulting in a tightly packed unit cell with the smallest observed volume and less than 3 Å between repeating pyridine units. The reduced steric size of BIP-H renders it the only ligand studied that packed in this fashion. Unit cells for the remaining ligands showed primarily $\pi-\pi$ interactions between aniline subunits on neighboring ligand

https://dx.doi.org/10.1021/acs.jpcc.0c06335
J. Phys. Chem. C 2020, 124, 22677−22683

molecules, resulting in larger values for the distance of interligand spacing and overall unit cell volumes for BIP-Me (3.7 Å spacing, 2099 Å^3 volume) and BIP-Ipr (4.5 Å spacing and 2900 Å^3 volume) ligands. Such a difference in packing and interligand distance affects the physical and electronic properties of QDs ligated with different BIP ligands, resulting in unique structure−activity relationships for the QDs depending on their environment (vide infra).

We summarize the basic spectroscopic characterization of QDs post ligand exchange in Figure 2, along with the results of

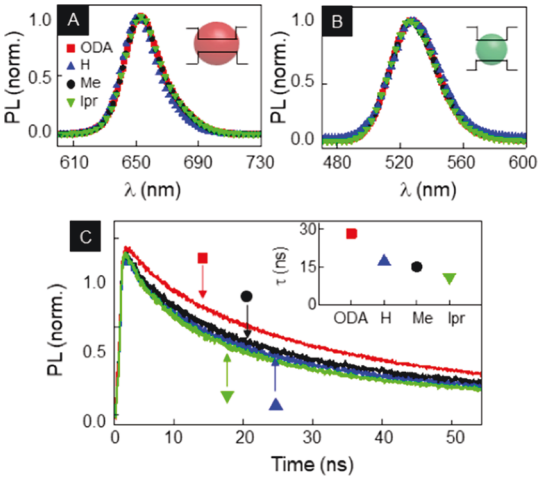

Figure 2. PL emission of (A) CZ640 and (B) CZ500 CdSe/ZnS QDs functionalized with ODA and the three BIP variations. (C) Time-resolved PL for all four populations of QD films deposited on an insulating glass substrate. (Inset) Recombination lifetime τ extracted from exponential fits to the data in the main part.

the ODA-ligated control dots for comparison. This is an important check because surface functionalization can cause changes in quantum confinement, which result in an emission red-shift, or proliferation of surface defects, which may accelerate core photo-oxidation and darkening. Photoluminescence (PL) of CZ640 and CZ500 nm QDs dispersed in solution shown in Figure 2A,B confirms that there are no significant changes to any aspect of the emission spectra after the ODA ligands are exchanged by the three variations of BIP. Photoluminescent quantum yield (PLQY) is another critical parameter that directly reflects the impact of ligand exchange. Our measurements do not reveal a significant difference in the PLQY between different QD populations. For ODA, H, Me, and IPr, the measured PLQYs are 35, 30, 36 and 32%, respectively. Time-resolved PL measurements of the QDs in a dilute solution further reveal no distinction between dots functionalized with ODA, BIP-H, BIP-Me, and BIP-Ipr, with the recombination time for all four populations being 40 ± 3 ns. Figure 2C plots the time-resolved PL curves for QD films deposited on a glass substrate, and the charge recombination lifetimes are calculated by first using a biexponential fit $I_{PL} = A_1e^{-t/\tau_1} + A_2e^{-t/\tau_2}$ and then using the results to extract the average lifetime $\tau = (A_1\tau_1^2 + A_2\tau_2^2)/(A_1\tau_1 + A_2\tau_2)$. These values are plotted in the inset and show a clear variation between the native ODA and the BIP ligands, where τ decreases from 30 ns for ODA-QDs to 11 ns for BIP-Ipr. Faster lifetimes are the norm when comparing QDs in films versus isolated QDs in dilute solutions, as interdot interactions allow additional routes of charge recombination. These mechanisms, the resulting timescales, and associated effects are strongly dependent on surface states and the subsequent modifications, a good overview of which has been previously described.[35−38] The most common mechanism is Forster resonant energy transfer (FRET), a dipole−dipole coupling where the efficiency $\varepsilon \sim 1/r^6$, r being the interdot separation.[38] These data would, therefore, suggest that the distance between QDs in the films, on average, decreases in ODA-, BIP-H-, BIP-Me-, and BIP-Ipr-functionalized QDs.

In an ensemble, FRET occurs as a result of the size inhomogeneity of the QDs, and the roles of donors and acceptors are satisfied by the smaller and larger dots in the population. As a result, the extent of FRET varies with wavelength of the emission spectrum. We verify this in Figure 3. Time-resolved PL curves for ODA-QDs with spectral

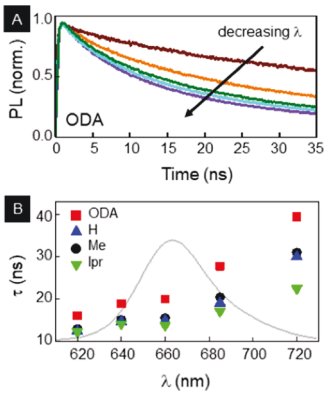

Figure 3. (A) Time-resolved PL curves at different spectral bands of the emission curve for the ODA-functionalized QD film. Lifetimes decrease with decreasing emission wavelength. (B) Spectrally resolved recombination times τ for all four QD films superposed on the corresponding spectral region over which they are evaluated.

resolution are plotted in Figure 3A, and the recombination can be seen to get faster as the emission wavelength at which the data are taken decreases. Figure 3B shows the extracted τ across the emission spectrum for all four differently ligated QDs. For ODA-QDs, we notice the expected variation of τ with wavelength, as well as the fact that at the long wavelength end, τ approaches the lifetime measured in solution. For the BIP-functionalized QDs, the trend is the same, but the shorter lifetimes even at the reddest end of the spectrum imply that the recombination is much faster than the solution values. This would indicate that there is some other route in addition to FRET, and the nature of aromatic ligands would suggest that to be charge transfer.

There remains the possibility that some of the difference in recombination between the ODA-QDs and the BIP-QDs may be because of the differences in interdot separation. To investigate that, we analyze the transmission electron microscopy (TEM) images of close-packed QD films, such as those shown in Figure 4A,B, for ODA and BIP-H functionalized QDs, respectively. For each type of QD, we generate a pair-distribution function (PDF) of its TEM image, as shown in Figure 4C, which plots the probability of finding a QD at a separation r from another QD. The first peak of this PDF is the average nearest-neighbor distance between the dots, and from this main figure which shows the PDF of ODA functionalized QDs, that distance is 8.3 nm. Similar analyses of the other QDs return varying QD separations and are plotted

https://dx.doi.org/10.1021/acs.jpcc.0c06335
J. Phys. Chem. C 2020, 124, 22677−22683

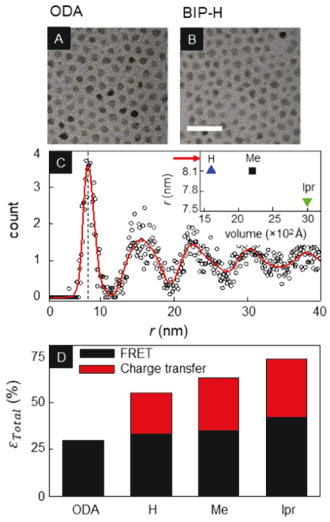

Figure 4. TEM images of drop-cast QD films with (A) ODA and (B) BIP-H ligands. Scale bar: 50 nm. (C) Radial distribution of interdot separation r obtained from TEM images and (inset) r values of the BIP variations plotted with the unit cell volume. Arrow indicates r for ODA-functionalized QDs. (D) Energy and charge transfer efficiencies for the four QD populations.

in the inset as a function of volume of the ligand unit cells. The inverse relation provides an interesting insight into the packing efficiency of the different ways the three BIP ligands stack. However, it also implies that there is a variation in FRET efficiency based on the ligand on the QDs. As shown in Figure 1C, the shape of the packing units (unit cells) is not uniform across the three BIPs studied. This shape disparity likely affects the mode of ligand stacking on QD surfaces, which should directly impact interdot separation.

We return to the averaged lifetimes of the QD films in the inset of Figure 2C and using τ of ODA-QDs in film and solution, calculate the efficiency $\varepsilon_{total} = 1 - \tau_{film}/\tau_{solution}$.[39] As ODA is insulating, it is reasonable that energy transfer is the only interdot interaction among these QDs, and given that, we extract the FRET constant R_o using $\varepsilon_{total} = \varepsilon_{FRET} = 1/1 + (r/R_o)^6$. R_o is defined as the separation where $\varepsilon_{FRET} = 50\%$ and is theoretically calculated using the overlap integral of the donor emission spectrum with the acceptor absorption spectrum and its mutual molecular orientation. Here, we evaluate it by equating the two expressions of ε_{FRET} and estimate $R_o = 7$ nm, which is very close to the rigorously calculated value of ~6.8 nm. Then, we calculate ε_{FRET} for the QDs ligated with the BIP ligands using this distance-dependent relation and the same R_o and when plotted in Figure 4D, it highlights that FRET does increase in the case of the BIP-functionalized QDs. However, when we calculate ε_{total} for the BIP-QDs using the formulation involving recombination times, those values are significantly greater than what is accounted for by FRET. For example, $\varepsilon_{total} = 54\%$ for BIP-H QDs but $\varepsilon_{FRET} = 33\%$. We attribute this difference to charge transfer, and calculate that efficiency $\varepsilon_{total} - \varepsilon_{FRET} = \eta$ to be 21% (BIP-H), 28% (BIP-Me), and 30% (BIP-Ipr) functionalized QDs. The increase of η between the different BIP ligands follows the trend of ε_{FRET} in them, both getting larger as interdot separation decreases in the QD films. To identify the nature and mechanism of charge transfer, we note that the BIP ligands are photogenerated hole-acceptors as their highest occupied molecular orbital (HOMO) aligns above the QD valence band. BIPs share similar structural elements to a well-known high efficiency hole acceptor, triazatruxene (TAT). The similarities between TAT and BIPs is significant with both molecules comprising of primarily SP2 hybridized carbons and nitrogens, as well as having extensive π character. This extensive π character is known to facilitate hole mobility and stabilize charged states through a reduction in the energy gap between the HOMO and lowest unoccupied molecular orbital bands. Along with extensive π π character, various heteroatoms (nitrogens) also facilitate charge stabilization.[40]

While inter-QD charge transfer is important or optimal device performance, efficient and fast charge extraction at electrodes or other interfaces is also a necessity. With this in mind, we investigate the recombination dynamics of the QD films when deposited on metallic and semiconducting substrates. The four differently ligated QDs are spin coated onto ITO-coated glass and on the optically polished n-type zinc oxide (n-ZnO) single crystalline sample. The recombination time τ for both sized QDs on the two substrates is shown in Figure 5A,B. For CZ500 (the smaller QDs with a larger

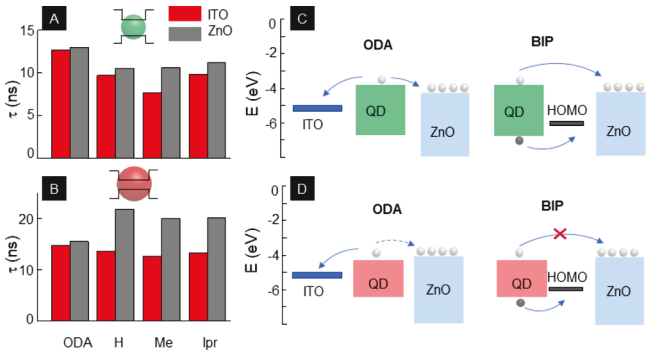

Figure 5. Recombination times τ for (A) CZ500 and (B) CZ640 QD films functionalized with ODA and the BIP ligands, when deposited on conducting ITO and semiconducting n-ZnO substrates. (C,D) Schematics sketching the charge transfer routes for the differently sized QDs.

bandgap), charge recombination times when ligated with ODA, while expectedly shorter than on glass, are nearly the same (12.6 and 13 ns) on ITO and ZnO. When functionalized with BIP variations, recombination does get faster for both substrates, which may be attributed to the charge delocalization of the aromatic rings resulting in a narrowing of the band gap between the QDs and substrates.[41−45] The schematics in Figure 5C demonstrates the relative band alignments of ITO and ZnO with the QD. The positional advantage of the QD conduction band makes electron transfer to either substrate energetically favorable when functionalized with ODA (Figure 5C, left). However, the hole-accepting nature of the BIP ligands allows both electrons and holes to be transferred away from the QD core, resulting in the faster recombination in the BIP-QDs (Figure 5C, right).

The same measurements for CZ640 QDs, which are larger and, therefore, have a smaller bandgap, have different results. For ODA, τ is again very similar on ITO and ZnO (14.7 and 15.3 ns, respectively). As the left schematic in Figure 5D shows, electron transfer to ITO is clearly favorable. Although the conduction band of ZnO ~0.1 eV is above that of the QD, stochastic electron transfer is allowed. BIP-QDs show a minor increase in electron transfer to ITO, driven again by the delocalized charges of the ligands. However, the change in the

https://dx.doi.org/10.1021/acs.jpcc.0c06335
J. Phys. Chem. C 2020, 124, 22677−22683

recombination rate when BIP-QDs are deposited on ZnO is both significant and unexpected. Recombination lifetimes of BIP-QDs are approximately 30% longer than that of ODA-QDs, indicating that functionalization by the BIP ligands, while facilitating hole transfer, somehow prevents electron transfer from the QD. As the excitation energy used in our studies is smaller than the wide bandgap of ZnO, the presence of oxygen vacancies makes as-grown ZnO highly *n*-doped. Therefore, a possibility is that the delocalized electron cloud of the BIP ligands not only interacts with the photogenerated electrons in the QD core, but also with those in the conduction band of ZnO. This has no consequence for the smaller QDs, where the difference between the energy levels of the QD core and ZnO drives electrons from the former to the latter. The near alignment of conduction bands in the case of the larger QDs and ZnO removes the advantage of this driving potential and concludes with the BIP ligands preventing electron extraction, while still allowing hole transfer. As a result, the recombination rate drops. This modulation of charge carrier transfer based on band alignment between the QDs and the substrates mediated by the BIP ligands is an interesting finding, as it opens up the possibility of tailoring functionalization based on specific needs of an application. An important point to note here is that while the charge transfer efficiency η in the QD films is ligand dependent, as shown in Figure 4D, in this demonstration of charge transfer from QDs to ITO and ZnO, there is little variation of the same with the different BIP ligands. We attribute this distinction to the fact that while charge transfer in the former is determined by inter-QD separation, for the latter the energetics control the efficiency. A second look at Figure 4D shows that η in the ascending order is IPr > Me > H, and as the inset in Figure 4C confirms, interdot separation follows H > Me > IPr. This is also the reason that no charge transfer is observed when the QDs are in solution. Transfer to substrates is nearly independent of which BIP ligand is used as the HOMO levels of all three are within 0.5 eV of each other and are, therefore, all nearly equivalently aligned with the QD valence band.

However, as mentioned earlier, the influence of ligands extends beyond that of transient charge transfer. Modification of QD surfaces may adversely affect long-term photostability of the QDs, and in Figure 6 we compare how functionalization with BIP ligands alters photoinduced effects. Figure 6A plots the spectrally integrated PL intensity for ODA-QDs over time under continuous photoexcitation. It increases rapidly for the first 20 min and then continues to rise at a slower rate. This photobrightening is a sign that there exist trap states within the bandgap of the core, most likely at the core−shell interface. Photogenerated carriers saturate these states, effectively deactivating nonradiative recombination centers, resulting in increasing PL. However, over the same time frame, the full width at half-maximum (fwhm) of the QD ensemble increases, which, coupled with a small blue-shift of the emission wavelength, suggests there is photo-oxidation of the QD core. As this reduces the core diameter, the size inhomogeneity of the ensemble is worsened, and the spectral width enhanced. In contrast, the photobrightening of BIP-H QDs stabilizes much faster and there is no observable increase in the emission fwhm over time. It is known that hole-accepting ligands can passivate QD surfaces more effectively than insulating ones[41] and our results confirm that here. It is also an important result as it demonstrates there are no detrimental long-term stability effects as a result of the BIP ligands.

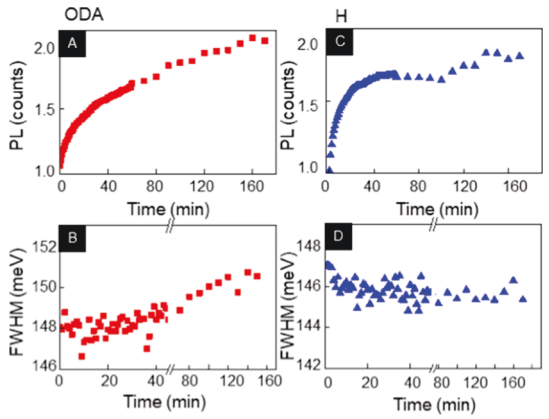

Figure 6. (A) Spectrally integrated PL intensity and (B) fwhm of the emission spectra for ODA-functionalized QDs under constant photoexcitation as a function of illumination time. (C) Spectrally integrated PL intensity and (B) fwhm of the emission spectra for BIP-H-functionalized QDs measured under the same conditions.

CONCLUSIONS

Heterogenous charge transfer has continued to be a critical area of advancement in science because of the increase in demand of society on technology that predicates itself off interfacial charge movement. The role of heterogenous charge transfer in modern conveniences such as smart phones to energy infrastructure cannot be under-represented. This importance on understanding heterogenous charge transfer has set the stage for this work and has shown both a novel and nuanced approach to modulate the kinetics of mesoscale heterogenous charge transfer. This was accomplished through the functionalizing semiconducting QDs with redox non-innocent (RNI) ligands as hole acceptors. Through non-standard application of these RNI ligands, controlled modulation of the charge transfer dynamics has been achieved on mesoscale materials. Moreover, this study has illuminated an intriguing band gap dependence on the photoluminescent recombination lifetimes, which can be observed across both deposited substrates of ITO and ZnO. While interesting, further work is needed in terms of characterizing the complex charge transfer dynamics as well as the effect of other RNI type ligands through tuning of the band gap.

METHODS

Representative Ligand Synthesis. BIP ligands were synthesized through azeotropic distillation of 2,6-diacetylpyridine in toluene with the corresponding aniline. 2,6-Diacetylpyridine (3 mmol), the aniline derivative (12 mmol), and *p*-toluenesulfonic acid (0.3 mmol) were added to a flame-dried 250 mL round bottom flask. Dry toluene (100 mL) was added and the resulting mixture was refluxed using a Dean−Stark apparatus for 24 h. The reaction mixture was cooled to room temperature and aqueous saturated sodium bicarbonate (100 mL) was added. This mixture was transferred to a separatory funnel and the organic layer was extracted. The aqueous layer was washed 3−4 times with dichloromethane and the organic layers were combined, dried with sodium sulfate, and concentrated. The resulting concentrate was dissolved in 15−20 mL of methanol and placed at −20 Celsius for approximately 12 h. The resulting yellow solid was

https://dx.doi.org/10.1021/acs.jpcc.0c06335
J. Phys. Chem. C 2020, 124, 22677−22683

vacuum filtered and washed with cold methanol. ^{1}H NMR was used to assess purity and recrystallization in cold methanol was performed if impurities were detected. Single crystals were grown through solvation in hot methanol and allowed to cool over night at room temperature.

Ligand Exchange. ODA-capped CdSe/ZnS QDs CZ640 (bandgap 1.91 eV) and CZ500 (bandgap 2.3 eV) were purchased from NN-Labs. CZ640 QDs have a core diameter of 4.8 nm (5−10% size inhomogeneity) and CZ500, a 2.0 nm core diameter (10−15% size inhomogeneity). Their surfaces were modified using BIP-H, BIP-Me, and BIP-Ipr. Surface exchange was carried out under inert conditions by adding the QDs to a hexane solution containing an excess of the modifying ligands relative to the native ODA. This solution is incubated for at least 5 min and then purified with acetonitrile (MeCN) and chloroform ($CHCl_3$). The QDs are then separated by centrifugation and dispersed in hexanes for optical measurements.

Sample Preparation. For analysis in solution, the QDs were housed in 2.5 mL glass vials. For measurements of QD films, the dots were spin coated onto glass, ITO, and *n*-ZnO (zinc oxide) substrates at 4500 rpm for 15 s, followed by annealing in an oven for 50 °C for 30 min.

Spectral Characterization. For static spectroscopy, we use a Princeton Instruments SP2300i spectrometer coupled to a thermoelectrically cooled deep depletion and low noise charge coupled detector, with a spectral resolution of 0.18 nm. An NKT Photonics Super-K laser tuned to 430 nm is used for excitation. For time-resolved measurements, the Super-K is set to a repetition rate of 26 MHz and the collected signal is first dispersed using the spectrometer, and then directed onto a single-photon avalanche diode coupled to a PicoHarp 300 time-correlated single photon counting system with an instrument response function of 28 ps.

Transmission Electron Microscopy. QD solutions were pipetted onto Pure C on 300 mesh Cu grids and left to dry overnight in an oven at 50 °C, then imaged in Thermo Fisher's Talos F200C G2 TEM.

■ ASSOCIATED CONTENT

Supporting Information

The Supporting Information is available free of charge at https://pubs.acs.org/doi/10.1021/acs.jpcc.0c06335.

Crystallographic information of BIP-H (CIF)

Crystallographic information of BIP-Me (CIF)

Crystallographic information of BIP-IPr (CIF)

■ AUTHOR INFORMATION

Corresponding Author

Ryan D. Baxter − *Department of Chemistry and Chemical Biology, School of Natural Sciences, University of California, Merced, California 95344, United States;* orcid.org/0000-0002-1341-5315; Email: rbaxter@ucmerced.edu

Authors

Mark D. Bartolo − *Department of Physics, School of Natural Sciences, University of California, Merced, California 95344, United States*

Ryan P. Brisbin − *Department of Chemistry and Chemical Biology, School of Natural Sciences, University of California, Merced, California 95344, United States*

James C. Fettinger − *Department of Chemistry, X-ray Crystallography Laboratory, University of California, Davis, California 95616, United States;* orcid.org/0000-0002-6428-4909

Sayantani Ghosh − *Department of Physics, School of Natural Sciences, University of California, Merced, California 95344, United States;* orcid.org/0000-0003-3440-7194

Complete contact information is available at: https://pubs.acs.org/10.1021/acs.jpcc.0c06335

Author Contributions

M.D.B. and R.P.B. contributed equally to the described work. The manuscript was written through contributions of all authors.

Notes

The authors declare no competing financial interest.

■ ACKNOWLEDGMENTS

This article is based upon work supported by the National Science Foundation under grant nos. NSF-CAREER 1752821 (R.D.B.) and NSF-CREST HRD-1547848 (S.G., M.D.B., and R.P.B.)

■ REFERENCES

(1) Moreels, I.; et al. Size-tunable, bright, and stable PbS quantum dots: A surface chemistry study. *ACS Nano* **2011**, *5*, 2004−2012.

(2) Wei, G.; et al. Size-tunable Lateral Confinement in Monolayer Semiconductors. *Sci. Rep.* **2017**, *7*, 3324.

(3) Fan, Q.; et al. Lead-Free Halide Perovskite Nanocrystals: Crystal Structures, Synthesis, Stabilities, and Optical Properties. *Angew. Chem., Int. Ed.* **2020**, *59*, 1030−1046.

(4) Grotevent, M. J.; et al. Nanoprinted Quantum Dot−Graphene Photodetectors. *Adv. Opt. Mater.* **2019**, *7*, 1900019.

(5) Livache, C.; et al. A colloidal quantum dot infrared photodetector and its use for intraband detection. *Nat. Commun.* **2019**, *10*, 2125.

(6) Sukhovatkin, V.; Hinds, S.; Brzozowski, L.; Sargent, E. H. Colloidal quantum-dot photodetectors exploiting multiexciton generation. *Science* **2009**, *324*, 1542−1544.

(7) Yu, S.; et al. Enhanced optical and thermal performance of white light-emitting diodes with horizontally layered quantum dots phosphor nanocomposites. *Photonics Res.* **2018**, *6*, 90.

(8) Cho, C.; Song, J. H.; Kim, C.; Jeong, S.; Lee, J. Y. Broadband light trapping strategies for quantum-dot photovoltaic cells (>10%) and their issues with the measurement of photovoltaic characteristics. *Sci. Rep.* **2017**, *7*, 17393.

(9) Khan, S. A.; Smith, G. T.; Seo, F.; Ellerbee, A. K. Label-free and non-contact optical biosensing of glucose with quantum dots. *Biosens. Bioelectron.* **2015**, *64*, 30−35.

(10) Tajarrod, N.; Rofouei, M. K.; Masteri-Farahani, M.; Zadmard, R. A quantum dot-based fluorescence sensor for sensitive and enzymeless detection of creatinine. *Anal. Methods* **2016**, *8*, 5911−5920.

(11) Brazhnik, K.; et al. Quantum dot-based lab-on-a-bead system for multiplexed detection of free and total prostate-specific antigens in clinical human serum samples. *Nanomed. Nanotechnol. Biol. Med.* **2015**, *11*, 1065−1075.

(12) Sukhanova, A.; et al. Oriented conjugates of single-domain antibodies and quantum dots: Toward a new generation of ultrasmall diagnostic nanoprobes. *Nanomed. Nanotechnol. Biol. Med.* **2012**, *8*, 516−525.

(13) Yang, X.; et al. Hydroiodic Acid Additive Enhanced the Performance and Stability of PbS-QDs Solar Cells via Suppressing Hydroxyl Ligand. *Nano-Micro Lett.* **2020**, *12*, 37.

(14) Chuang, C.-H. M.; Brown, P. R.; Bulović, V.; Bawendi, M. G. Improved performance and stability in quantum dot solar cells through band alignment engineering. *Nat. Mater.* **2014**, *13*, 796−801.
(15) Choi, M.-J.; et al. Cascade surface modification of colloidal quantum dot inks enables efficient bulk homojunction photovoltaics. *Nat. Commun.* **2020**, *11*, 103.
(16) Krivenkov, V.; et al. Ligand-Mediated Photobrightening and Photodarkening of CdSe/ZnS Quantum Dot Ensembles. *J. Phys. Chem. C* **2018**, *122*, 15761−15771.
(17) Zhang, Y.; Clapp, A. Overview of stabilizing ligands for biocompatible quantum dot nanocrystals. *Sensors* **2011**, *11*, 11036−11055.
(18) Cao, Y.; Stavrinadis, A.; Lasanta, T.; So, D.; Konstantatos, G. The role of surface passivation for efficient and photostable PbS quantum dot solar cells. *Nat. Energy* **2016**, *1*, 16035.
(19) Hines, D. A.; Kamat, P. V. Quantum dot surface chemistry: Ligand effects and electron transfer reactions. *J. Phys. Chem. C* **2013**, *117*, 14418−14426.
(20) Seker, F.; Meeker, K.; Kuech, T. F.; Ellis, A. B. Surface chemistry of prototypical bulk II-VI and III-V semiconductors and implications for chemical sensing. *Chem. Rev.* **2000**, *100*, 2505−2536.
(21) Yoshihara, T.; Druzhinin, S. I.; Zachariasse, K. A. Fast intramolecular charge transfer with a planar rigidized electron donor/acceptor molecule. *J. Am. Chem. Soc.* **2004**, *126*, 8535−8539.
(22) Slama-Schwok, A.; Blanchard-Desce, M.; Lehn, J. M. Intramolecular charge transfer in donor-acceptor molecules. *J. Phys. Chem.* **1990**, *94*, 3894−3902.
(23) Tamai, K.; et al. Visible-Light Selective Photooxidation of Aromatic Hydrocarbons via Ligand-to-Metal Charge Transfer Transition on Nb2O5. *J. Phys. Chem. C* **2017**, *121*, 22854−22861.
(24) Sevov, C. S.; et al. Physical Organic Approach to Persistent, Cyclable, Low-Potential Electrolytes for Flow Battery Applications. *J. Am. Chem. Soc.* **2017**, *139*, 2924.
(25) Chirik, P. J.; Wieghardt, K. Radical ligands confer nobility on base-metal catalysts. *Science* **2010**, *327*, 794.
(26) Kaim, W. Manifestations of noninnocent ligand behavior. *Inorg. Chem.* **2011**, *50*, 9752.
(27) Small, B. L.; Brookhart, M.; Bennett, A. M. A. Highly active iron and cobalt catalysts for the polymerization of ethylene [18]Highly Active Iron and Cobalt Catalysts for the Polymerization of Ethylene. *J. Am. Chem. Soc.* **1998**, *120*, 4049.
(28) Lyaskovskyy, V.; De Bruin, B. Redox non-innocent ligands: Versatile new tools to control catalytic reactions. *ACS Catal.* **2012**, *2*, 270.
(29) Docherty, J. H.; Peng, J.; Dominey, A. P.; Thomas, S. P. Activation and discovery of earth-abundant metal catalysts using sodium tert-butoxide. *Nat. Chem.* **2017**, *9*, 595.
(30) Bol, A. A.; Meijerink, A. Luminescence Quantum Efficiency of Nanocrystalline ZnS:Mn2+. 2. Enhancement by UV Irradiation. *J. Phys. Chem. B* **2001**, *105*, 10203−10209.
(31) Xu, L.; Chen, K.; El-Khair, H. M.; Li, M.; Huang, X. Enhancement of band-edge luminescence and photo-stability in colloidal CdSe quantum dots by various surface passivation technologies. *Appl. Surf. Sci.* **2001**, *172*, 84−88.
(32) Yoo, D.; et al. Origin of the Stability and Transition from Anionic to Cationic Surface Ligand Passivation of All-Inorganic Cesium Lead Halide Perovskite Nanocrystals. *J. Phys. Chem. Lett.* **2020**, *11*, 652−658.
(33) Frederick, M. T.; Weiss, E. A. Relaxation of exciton confinement in CdSe quantum dots by modification with a conjugated dithiocarbamate ligand. *ACS Nano* **2010**, *4*, 3195−3200.
(34) Bart, S. C.; Lobkovsky, E.; Chirik, P. J. Preparation and molecular and electronic structures of iron(0) dinitrogen and silane complexes and their application to catalytic hydrogenation and hydrosilation. *J. Am. Chem. Soc.* **2004**, *126*, 13794.
(35) Zhang, J.; Tolentino, J.; Smith, E. R.; Zhang, J.; Beard, M. C.; Nozik, A. J.; Johnson, J. C. Carrier Transport in PbS and PbSe QD Films Measured by Photoluminescence Quenching. *J. Phys. Chem. C* **2014**, *118*, 16228−16235.
(36) Zhao, K.; Pan, Z.; Zhong, X. Charge Recombination Control for High Efficiency Quantum Dot Sensitized Solar Cells. *J. Phys. Chem. Lett.* **2016**, *7*, 406−417.
(37) Tagliazucchi, M.; Tice, D. B.; Sweeney, C. M.; Morris-Cohen, A. J.; Weiss, E. A. Ligand-Controlled Rates of Photoinduced Electron Transfer in Hybrid CdSe Nanocrystal/Poly(viologen) Films. *ACS Nano* **2011**, *5*, 9907−9917.
(38) Crooker, S. A.; Hollingsworth, J. A.; Tretiak, S.; Klimov, V. I. Spectrally Resolved Dynamics of Energy Transfer in Quantum-Dot Assemblies: Towards Engineered Energy Flows in Artificial Materials. *Phys. Rev. Lett.* **2002**, *89*, 186802.
(39) Rodarte, A. L.; Pandolfi, R. J.; Ghosh, S.; Hirst, L. S. Quantum dot/liquid crystal composite materials: self-assembly driven by liquid crystal phase transition templating. *J. Mater. Chem. C* **2013**, *1*, 5527−5532.
(40) Urieta-Mora, J.; García-Benito, I.; Molina-Ontoria, A.; Martín, N. Hole transporting materials for perovskite solar cells: a chemical approach. *Chem. Soc. Rev.* **2018**, *47*, 8541−8571.
(41) Lyaskovskyy, V.; de Bruin, B. Redox Non-Innocent Ligands: Versatile New Tools to Control Catalytic Reactions. *ACS Catal.* **2012**, *2*, 270−279.
(42) Kaim, W. The shrinking world of innocent ligands: Conventionaland non-conventional redox-active ligands. *Eur. J. Inorg. Chem.* **2012**, *2012*, 343−348.
(43) Pitchaiya, S.; et al. A review on the classification of organic/inorganic/carbonaceous hole transporting materials for perovskite solar cell application. *Arabian J. Chem.* **2020**, *13*, 2526−2557.
(44) Urieta-Mora, J.; García-Benito, I.; Molina-Ontoria, A.; Martín, N. Hole transporting materials for perovskite solar cells: a chemical approach. *Chem. Soc. Rev.* **2018**, *47*, 8541−8571.
(45) Tan, Y.; Jin, S.; Hamers, R. J. Influence of hole-sequestering ligands on the photostability of CdSe quantum dots. *J. Phys. Chem. C* **2013**, *117*, 313−320.

https://dx.doi.org/10.1021/acs.jpcc.0c06335
J. Phys. Chem. C 2020, 124, 22677−22683